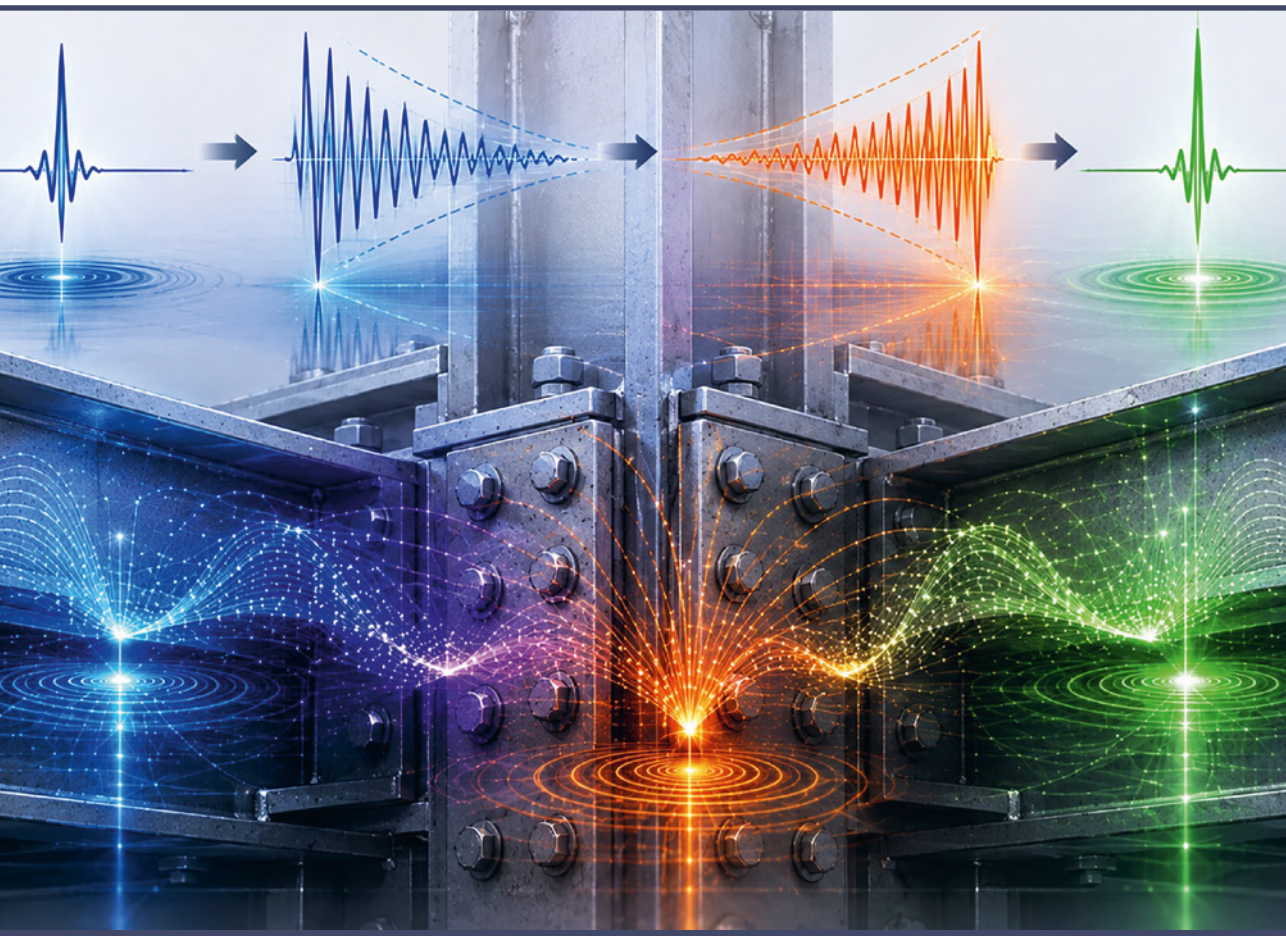
RIGA TECHNICAL UNIVERSITY

Viktors Kurtenoks

MULTIDIMENSIONAL ASSESSMENT OF STRUCTURAL JOINT INTEGRITY VIA AXIS-MATCHED RESPONSE CORRELATION ENHANCED BY TIME-REVERSAL IMPACT FOCUSING

Summary of the Doctoral Thesis



RTU Press
Riga 2026

RIGA TECHNICAL UNIVERSITY
Faculty of Civil and Mechanical Engineering
Institute of High-Performance Materials and Structures

Viktors Kurtenoks
Doctoral Student of the Study Programme "Civil Engineering"

MULTIDIMENSIONAL ASSESSMENT OF STRUCTURAL JOINT INTEGRITY VIA AXIS-MATCHED RESPONSE CORRELATION ENHANCED BY TIME-REVERSAL IMPACT FOCUSING

Summary of the Doctoral Thesis

Scientific supervisors

Professor Dr. sc. ing.
JEVGENIJS BARKANOVS

Dr. sc. ing.
ALEKSEJS TATARINOVS

RTU Press
Riga 2026

Kurtenoks, V. Multidimensional Assessment of Structural Joint Integrity via Axis-Matched Response Correlation Enhanced by Time-Reversal Impact Focusing. Summary of the Doctoral Thesis. – Riga: RTU Press, 2026. – 46 p.

Published in accordance with the decision of the Promotion Council "RTU P-06" of 17 August 2026, Minutes No. 04030-9.6/22.

The cover image was created by the author using generative artificial intelligence tools.

https://doi.org/10.7250/9789934373640
ISBN 978-9934-37-364-0 (pdf)

DOCTORAL THESIS PROPOSED TO RIGA TECHNICAL UNIVERSITY FOR PROMOTION TO THE SCIENTIFIC DEGREE OF DOCTOR OF SCIENCE

To be granted the scientific degree of Doctor of Science (PhD), the present Doctoral Thesis has been submitted for defence at the open meeting of the RTU Promotion Council on 27 November 2026 at 14:00 at the Faculty of Civil and Mechanical Engineering of Riga Technical University, Ķīpsalas iela 6A, Room 538.

OFFICIAL REVIEWERS

Professor Dr. sc. ing. Aleksandrs Korjakins
Riga Technical University

Professor Dr. habil. sc. ing. Igor Kabashkin
Transport and Telecommunication Institute, Latvia

Professor Dr. Raimondas Pomarnacki
Vilnius Gediminas Technical University, Lithuania

DECLARATION OF ACADEMIC INTEGRITY

I hereby declare that the Doctoral Thesis submitted for review to Riga Technical University for promotion to the scientific degree of Doctor of Science (PhD) is my own. I confirm that this Doctoral Thesis has not been submitted to any other university for promotion to a scientific degree.

Viktors Kurtenoks ……. (signature)
Date: ……

The Doctoral Thesis has been written in English. It consists of an Abstract, 7 chapters, 18 figures, 2 tables, and 9 appendices; the total number of pages is 138, including appendices. The Bibliography contains 33 titles.

ANNOTATION

Reliable assessment of structural joint integrity is essential for ensuring the safety and serviceability of engineering structures, yet existing diagnostic approaches in structural health monitoring frequently suffer from directionally incomplete observability. Most methods are effectively one-dimensional in sensing or, when multiaxial sensing is employed, still rely on excitation that does not ensure a controlled multidimensional response around the point of interest. As a result, early-stage, axis-selective degradation signatures may remain undetected, limiting the diagnostic reliability of current practice.

This Doctoral Thesis, through publications, develops and experimentally validates a synchronized multidimensional diagnostic approach designed to overcome these limitations. The core innovation lies in the systematic integration of five interdependent components: paired three-dimensional acceleration measurements on opposite sides of a structural joint within a shared time-reversal-focused response domain, controlled multidimensional excitation based on time-reversal wave-focusing principles, synchronized excitation and sensing channels, per-axis coherence evaluation between paired opposite-side acceleration responses, and fusion of directional indicators into a single scalar metric of joint condition.

The Thesis is supported by three complementary publication groups forming a unified research trajectory. The first group establishes axis-matched multiaxial response measurements, correlation-based indicators, scalar-metric fusion, and degradation emulation across different structural objects and materials. The second group provides the time-reversal wave-focusing basis required to extend response comparison toward controlled multidimensional excitation. The third group addresses high-precision timing and multichannel synchronization methods required to enable consistent time-reversal focusing in distributed measurement systems with digitally connected sensors and long-distance noise-immune transmission lines. Together, these groups form the methodological basis of the proposed approach, in which multiaxial response evaluation, excitation control, and time-consistent distributed sensing are treated as interconnected components of a single structural joint diagnostic methodology.

The integrated methodology is validated through a synchronized, multidimensional structural joint experiment that emulates progressive degradation via controlled bolt-torque reduction over eight stages. The results demonstrate that controlled multidimensional excitation improves directional observability, reduces axis-dependent response ambiguity, and enhances response reproducibility under progressive degradation conditions. The fused Multiaxial Component Coherence Metric (MCCM) exhibits a monotonic decrease across all degradation stages, providing a diagnostic sensitivity that individual single-axis indicators cannot consistently achieve.

The methodological components are documented in eight scientific publications and one granted patent. This Thesis integrates hardware design, synchronization, wave-based excitation control, and multiaxial structural response evaluation into a reproducible framework for the non-destructive assessment of structural joints.

CONTENTS

LIST OF ABBREVIATIONS 7
CHAPTER 1. OVERVIEW 8
1.1. Introduction 8
1.2. State of the Art 8
1.2.1. Localized Joint Diagnostic Approaches 9
1.2.2. Response Comparison and Multiaxial Observability 10
1.2.3. Time-Reversal Methods and Axis-Specific Excitation Control 10
1.2.4. Distributed Acquisition and Synchronization 11
1.2.5. Research Gap 11
1.3. Aim of Research 12
1.4. Main Statement 12
1.5. Scientific Novelty 12
1.6. Research Objectives 13
1.7. Structure of the Thesis 13
1.8. Publications and Scientific Dissemination 14
CHAPTER 2. METHODOLOGICAL SCOPE AND PREREQUISITES 17
2.1. Measured Quantities and Scale Treatment 17
2.2. Experimental Objects 17
2.3. Sensor Configuration and Positioning Requirements 17
2.3.1. Virtual Coaxial Alignment Requirement 18
2.3.2. Effect on Waveform Comparability (RCR) 18
2.3.3. Effect on Time-Reversal Defocusing 19
2.3.4. Practical Bandwidth Criterion for Sensor Spacing 20
2.4. Actuator Configuration and Positioning Requirements 20
2.5. Degradation Emulation 21
2.6. Time-Reversal Impact Focusing Principles 21
2.7. Multidimensional Time-Reversal Impact Focusing (MTRIF) 23
2.8. Time-Domain Coherence Prerequisite and CNSS Rationale 25
2.9. Response Coherence Ratio (RCR) 26
2.10. Multiaxial Component Coherence Metric (MCCM) 27
CHAPTER 3. HARDWARE–SOFTWARE PLATFORM FOR DATA ACQUISITION 28

3.1. Purpose and Scope of the Platform 28
3.2. System Overview and Core Architecture 28
3.3. Excitation Subsystem 29
3.4. Sensing, Acquisition, and Noise-Robust Data Transfer 29
3.5. Time-Reference Support and CNSS Observables 30
3.6. Control Software and User Interface 30
3.7. Key Specifications of the Platform 31
CHAPTER 4. DATA COLLECTION 32
4.1. Baseline Object and Joint Configuration 32
4.1.1. Sensor Placement 33
4.1.2. Actuator Placement 33
4.1.3. Degradation Method 33
4.2. Measurement Steps 33
CHAPTER 5. SIGNAL PROCESSING AND METRIC EVALUATION 35
5.1. Per-Axis RCR Evaluation 35
5.2. MCCM Computation 36
CHAPTER 6. METRIC EVALUATION RESULTS 37
6.1. Per-Axis RCR Repeatability Across Five Measurement Cycles 37
6.2. MCCM Repeatability and Degradation Trend 38
6.3. Dispersion Analysis of RCR and MCCM 38
CHAPTER 7. FINAL REMARKS 41
7.1. Main Conclusions 41
7.2. Practical Recommendations 41
7.3. Further Development 42
7.4. Limitations of the Current Study 42
ACKNOWLEDGEMENT 44
REFERENCES 45

LIST OF ABBREVIATIONS

Abbreviation	Explanation of Abbreviation
3DOF	Three Degrees of Freedom
6DOF	Six Degrees of Freedom (three linear and three rotational axes)
AMR	Axis-Matched Response
CNSS	Cross-Node Sample Synchronization
FPGA	Field-Programmable Gate Array
I²S	Inter-IC Sound
IMU	Inertial Measurement Unit
LVDS	Low-Voltage Differential Signaling
MCCM	Multiaxial Component Coherence Metric
MTRIF	Multidimensional Time-Reversal Impact Focusing
POI	Point of Interest
RCM	Response-Comparison Metric
RCR	Response Coherence Ratio
RMS	Root Mean Square
SHM	Structural Health Monitoring
SPI	Serial Peripheral Interface
TR	Time Reversal
USB	Universal Serial Bus

CHAPTER 1. OVERVIEW

1.1. Introduction

Structural joint diagnostics in SHM are frequently limited by incomplete observability when single-axis sensing and excitation are employed. Because joint degradation can be axis-selective, early-stage damage may manifest along specific translational components while remaining weakly expressed or undetected along others. Multiaxial sensing alone is insufficient when excitation remains effectively one-dimensional, as it does not reliably stimulate the full directional response field around the joint. Simply increasing impact energy is not a viable alternative, since it may introduce nonlinear effects, reduce repeatability, and overstress the joint interface.

To overcome these limitations, this Thesis develops a diagnostic framework that shifts the focus toward controlled multidimensional joint assessment. The framework begins by acquiring three Axis-Matched Response (AMR) pairs from 3DOF sensors mounted on opposite sides of the joint. To ensure that these AMR components are obtained under controlled multidimensional excitation conditions, Multidimensional Time-Reversal Impact Focusing (MTRIF) is used to synthesize a virtual impact point at the near-sensor location, producing triaxial linear excitation. This multidimensional interaction is supported by Cross-Node Sample Synchronization (CNSS), which maintains the sample-level temporal consistency required for waveform-level comparison. The framework then uses the Response Coherence Ratio (RCR) to evaluate the pointwise coherence of each AMR pair. Finally, the three RCR values are fused into the Multiaxial Component Coherence Metric (MCCM), providing a scalar indicator that reduces axis-dependent dispersion and supports interpretation of the joint structural condition.

1.2. State of the Art

This section critically reviews structural-joint SHM methods relevant to localized wave-based and vibration-based diagnostics. The review concentrates on active diagnostic approaches in which excitation is introduced into the structure and the measured response is used to assess degradation-related changes at the monitored joint. Global modal monitoring methods and general condition-monitoring systems are considered only as contextual background where they help clarify the limitations of localized joint diagnostics. The literature search was conducted using the Scopus and Web of Science databases with search terms including combinations of “structural joint,” “bolted joint monitoring,” “time reversal,” “structural health monitoring,” “multiaxial sensing,” “waveform comparison,” and “vibration-based diagnostics.” The search was supplemented by forward and backward citation tracking from key references.

The reviewed literature was selected according to three inclusion criteria. First, the study had to be relevant to structural joints, including bolted, bonded, riveted, composite, lap-joint, or similar connection regions. Second, the method had to involve an active wave- or vibration-based diagnostic scheme, where excitation is introduced into the structure, and the response is

analyzed after interaction with the monitored joint. Third, the diagnostic information had to be related to degradation-induced changes in the local dynamic behavior of the monitored joint, including stiffness, coupling, wave propagation, or response transfer characteristics.

Time-Reversal (TR) studies are considered as a separate group because TR focusing is one of the enabling principles of the proposed framework; therefore, selected works beyond structural-joint SHM are included, where they provide methodological background for controlled replay, focusing, or multi-emitter excitation.

The selected studies were analyzed according to the following methodological criteria.

1. Cross-joint response acquisition – whether responses are measured on both sides of the structural joint, allowing degradation to be evaluated through changes in dynamic coupling between the connected structural elements.
2. Excitation directional diversity – whether excitation activates only one dominant direction or propagation path or provides controlled excitation diversity capable of stimulating several directional response components near the joint.
3. Sensing dimensionality and multichannel interpretation – whether the response is measured using single-axis or multiaxial sensing, and whether multiple response components are interpreted independently or fused into a combined diagnostic indicator.
4. Cross-joint waveform comparison – whether the method compares full waveform responses measured on opposite sides of the joint, rather than relying only on scalar energy, modal, impedance, or spectral indicators.
5. Time-reversal axis-specific excitation – whether TR replay is used as a general focusing procedure, or whether separate axis-specific replay conditions are formed to control excitation of the receiving point along the measured response axes.
6. Distributed acquisition and synchronization – whether the sensing architecture uses centralized acquisition, short-range analog wiring, or distributed digital nodes, and whether synchronization is explicitly maintained at the sample level.

These criteria are not used to rank the reviewed studies by general SHM performance. They are used to identify which methodological requirements are already addressed in the literature and which remain insufficiently integrated for localized multidimensional structural-joint diagnostics. The following subsections discuss the reviewed works against these criteria.

1.2.1. Localized Joint Diagnostic Approaches

Frequency-response, guided-wave, and impedance-based approaches constitute the main body of localized structural-joint diagnostics. Frequency-response and transfer-based methods evaluate joint degradation through changes in dynamic characteristics between excitation and response locations. Tol and Özgüven [1] demonstrated that bolted-joint loosening modifies local transfer characteristics and vibration-response behavior, while related frequency-response comparison and cross-signature approaches were investigated in [2]. Guided-wave and Lamb-wave methods provide stronger localization capability because they are sensitive to wave interaction with joint degradation. Such approaches were applied to composite bolted joints, bolted-joint degradation, active piezoelectric sensing, and diffuse-wave or guided-wave monitoring of loosening and degradation [3–7].

Electromechanical impedance methods estimate joint condition through changes in local electromechanical coupling between piezoelectric transducers and the monitored structure [8–11]. These approaches provide high local sensitivity to stiffness and coupling variation near the

joint. However, when assessed against the criteria defined above, these methods typically rely on scalar indicators, limited propagation paths, or directionally constrained actuator–receiver configurations. Their principal limitation is therefore not insufficient damage sensitivity per se; rather, it is the incomplete integration of cross-joint multiaxial acquisition, controlled excitation diversity, and waveform-level near/far response comparison. For example, while guided-wave methods [3, 4] can detect bolt loosening through changes in wave propagation, they typically evaluate a single propagation path and do not capture the full three-dimensional response of the joint region. Similarly, impedance-based methods [8–10] provide high local sensitivity but measure changes in electromechanical coupling at a single transducer location without cross-joint response comparison.

1.2.2. Response Comparison and Multiaxial Observability

Several studies show that degradation-sensitive information can be extracted by comparing dynamic responses measured at different structural locations [1, 2, 6]. Such approaches reduce dependence on detailed analytical models, relying instead on experimentally observed changes in response induced by degradation. Earlier studies associated with the present Thesis [12–15] investigated localized response-comparison strategies using paired multiaxial response acquisition near structural joints. These studies demonstrated that degradation-sensitive behavior may appear differently across measurement directions depending on joint geometry, wave propagation paths, and excitation conditions.

Multiaxial sensing increases the directional information available from the structure, and six-degree-of-freedom and multichannel sensing concepts have been investigated for structural monitoring applications [16, 17]. However, multiaxial sensing alone does not guarantee complete observability of the degradation state. If excitation remains effectively direction-limited, some response components may be weakly activated, and degradation-sensitive changes may remain hidden or unstable in individual channels. The key methodological issue is therefore not merely whether multiple response components are measured, but whether they are measured on both sides of the joint under excitation conditions that activate the relevant directional response field.

1.2.3. Time-Reversal Methods and Axis-Specific Excitation Control

Time-reversal (TR) methods provide a mechanism for wavefield refocusing based on reciprocity [18]. By replaying time-reversed responses through the original propagation paths, wave energy can be concentrated near a selected point of interest. In the context of this Thesis, the key question is not merely whether TR focusing is applied, but whether replay conditions are formed in an axis-specific manner such that the receiving point is excited along the measured response axes.

TR techniques have been applied to structural-condition assessment and joint diagnostics in several studies [19–25]. These studies demonstrate that TR replay can improve localization and sensitivity to joint-related changes. However, most reported implementations remain limited to excitation directions, constrained propagation paths, or single-component response evaluation. They generally do not employ TR replay to form axis-specific excitation conditions combined with synchronized multiaxial near/far waveform comparison across the joint. For instance, Du et al. [20, 23] demonstrated bolt-preload monitoring using virtual time-reversal

focusing, but the excitation and sensing remained confined to a single propagation direction. Wang and Song [24] combined vibro-acoustic modulation with time reversal for bolt loosening detection, yet the method evaluated only a single modulation index rather than multiaxial waveform coherence.

Earlier studies by the author and collaborators [26–29] investigated multi-emitter TR focusing in acoustical systems operating in attenuative propagation environments. These studies are not treated here as structural-joint diagnostic works; rather, they serve as methodological precursors demonstrating that coordinated replay from multiple emitters can concentrate wave energy near a selected spatial location. This principle supports the transition toward controlled axis-specific and multidirectional excitation in localized structural-joint diagnostics.

1.2.4. Distributed Acquisition and Synchronization

Distributed sensing architectures are becoming increasingly relevant for practical SHM systems [16, 30]. However, many waveform-sensitive methods, including TR replay and direct waveform comparison, have been demonstrated in centralized laboratory configurations in which excitation and acquisition share a common timing domain. In such configurations, synchronization is implicitly ensured by common acquisition hardware or by short-range analog sensor wiring.

This assumption becomes problematic when sensing nodes are spatially distributed and digitize signals independently. Independent sampling clocks introduce systematic offset and thermal drift. For scalar or slowly varying indicators, such timing errors may be less critical. For waveform-level comparison, TR replay, and pointwise coherence evaluation, however, timing inconsistency directly affects waveform shape, phase relations, replay consistency, and inter-channel comparability. The synchronization requirements become particularly stringent when TR focusing is used for controlled axis-specific excitation, because timing errors reduce the quality and repeatability of the focused response. Most existing TR-based SHM studies either assume ideal synchronization or operate in centralized configurations where this assumption is implicitly satisfied.

Synchronization-related studies associated with the present study [31–33] investigated timing stability, temporal reconstruction, and sample-consistency maintenance in distributed multichannel acquisition systems. These studies provide the technical basis for maintaining waveform-level consistency when excitation and sensing nodes are separated.

1.2.5. Research Gap

The reviewed literature demonstrates substantial progress in localized structural-joint diagnostics. Existing studies provide damage-sensitive methods based on frequency-response variation, guided waves, impedance changes, response comparison, TR focusing, multiaxial sensing, and distributed acquisition.

However, these methodological elements have predominantly been investigated in isolation. The reviewed works do not sufficiently integrate controlled axis-specific multidirectional excitation, paired cross-joint multiaxial response acquisition, waveform-level near/far response comparison, sample-level synchronization, and fused multichannel interpretation within a single diagnostic chain.

This limitation defines the research gap addressed by the present Thesis. To bridge this gap, the proposed framework integrates multidirectional time-reversal excitation focusing, paired near/far 3DOF sensing, synchronized waveform-level response comparison, per-axis coherence evaluation, and fused multichannel interpretation into a unified methodology for localized structural-joint assessment.

1.3. Aim of Research

The aim of this research is to develop and experimentally validate a multidimensional methodology for structural joint integrity assessment that integrates controlled axis-specific excitation, synchronized cross-joint multiaxial sensing, and waveform-level coherence evaluation.

The proposed approach uses multidimensional time-reversal impact focusing (MTRIF) to synthesize an axis-specific virtual impact at the near-sensor location using spatially distributed actuators. The structural condition of the joint is evaluated through three axis-matched response (AMR) pairs measured by near and far 3DOF sensors mounted on opposite sides of the joint. Per-axis coherence is quantified using the response coherence ratio (RCR), and the resulting values are fused into the multiaxial component coherence metric (MCCM).

1.4. Main Statement

The research hypothesis of this Thesis was delineated as follows.

1. Structural joint degradation can be more completely characterized through multiaxial response analysis of axis-matched response pairs (AMR) measured on opposite sides of the joint than through single-point, unidirectional response evaluation.
2. Physically meaningful AMR pair analysis requires a controlled multidimensional response field in the analyzed joint region, which can be synthesized by multidimensional time-reversal impact focusing (MTRIF).
3. Reliable implementation of the AMR–MTRIF structural joint assessment methodology is not possible without precise synchronization between excitation and sensing nodes, which is achieved in this Thesis by cross-node sample synchronization (CNSS).

1.5. Scientific Novelty

1. The novelty lies in the formation of a controlled multiaxial response field in the analyzed joint region by means of multidimensional time-reversal impact focusing (MTRIF).
2. A new approach has been developed and validated for the per-axis evaluation of three directionally specific axis-matched response (AMR) pairs within a common MTRIF-focused response region.

3. A novel integrated methodological framework has been formulated, developed, and validated for multidimensional structural joint diagnostics by combining MTRIF, AMR, and cross-node sample synchronization (CNSS), where CNSS is treated as the key enabling component required for reliable framework operation.

1.6. Research Objectives

To achieve the stated research aim, the following objectives are established.

1. To develop a synchronized hardware–software platform implementing cross-node sample synchronization (CNSS) to ensure continuous sample-level alignment between excitation and sensing nodes under temporal and thermal variations.
2. To implement multidimensional time-reversal impact focusing (MTRIF) using a multi-actuator configuration in order to synthesize an axis-specific virtual impact at the near-sensor location.
3. To establish a paired cross-joint 3DOF sensing scheme using near and far sensors mounted on opposite sides of the joint and to form three axis-matched response (AMR) pairs from matched linear acceleration components.
4. To develop a per-axis waveform-level coherence evaluation procedure based on the response coherence ratio (RCR) for the three AMR pairs under progressive degradation.
5. To formulate the multiaxial component coherence metric (MCCM) as a fused scalar indicator combining the three per-axis RCR values to reduce axis-dependent dispersion and improve diagnostic interpretability.
6. To experimentally validate the integrated framework on a baseline structural joint under progressive degradation conditions and to relate the final methodology to supporting experimental evidence reported in the appended publications.

1.7. Structure of the Thesis

The Thesis consists of seven chapters. Chapter 1 outlines the problem of structural joint diagnostics, reviews the current literature, and defines the research aim, main statements, scientific novelty, and objectives. Chapter 2 defines the methodological scope, including the 3DOF sensing requirements, the MTRIF concept, the CNSS rationale, and the formal definitions of AMR, RCR, and MCCM. Chapter 3 describes the hardware–software platform, including the system architecture, excitation subsystem, sensing chain, and synchronization implementation. Chapter 4 presents the experimental setup and data-collection workflow, including sensor and actuator placement, degradation stages, and dataset composition. Chapter 5 details the signal-processing and metric-calculation procedures, focusing on triaxial RCR evaluation and MCCM fusion. Chapter 6 presents the metric-evaluation results, including per-axis RCR trends and fused MCCM behavior across degradation stages. Chapter 7 summarizes the findings, provides practical recommendations, and outlines directions for further development.

The publications forming the basis of the Thesis are listed in Section 1.8, while the main chapters synthesize their methodological contributions into a unified diagnostic framework.

1.8. Publications and Scientific Dissemination

This Thesis is based on eight scientific publications [12–15, 27, 31–33] and one granted patent. The appended publications do not represent independent or unrelated studies; rather, they document the progressive development of the methodological and engineering components synthesized in this Thesis into a unified framework for localized structural-joint diagnostics.

The research trajectory began with response-comparison methods for structural joints. The study on coaxial acceleration correlation for structural-joint quality assessment [12] introduced the principle of comparing vibration responses measured in three spatial directions using coaxially oriented 3D accelerometers placed at different parts of a structural joint. The related non-model vibration analysis study [13] supported the use of experimentally observed response changes rather than detailed analytical models as the basis for structural-joint assessment. These publications established the initial methodological direction developed further in Chapter 2 as paired near/far response acquisition and in Chapter 5 as waveform-level metric evaluation.

The next stage extended this concept toward multiaxial structural-joint diagnostics under degradation. The study on non-destructive damage detection by coaxial correlation in 6D space [14] presented paired multiaxial sensing on opposite sides of a structural joint, synchronized excitation–response acquisition, repeated measurements, averaging, and similarity-based evaluation for monitoring degradation. The timber-joint study [15] further demonstrated that response comparison between sensors placed on different sides of a joint can be used to assess degradation in timber structural connections. Together, these publications demonstrated that degradation-sensitive response behavior may differ across measurement directions, thereby supporting the need for per-axis evaluation and fused multichannel interpretation. In this Thesis, these earlier concepts are formalized as axis-matched response (AMR) pairs, response coherence ratio (RCR), and multiaxial component coherence metric (MCCM), described in Chapters 2 and 5 and evaluated in Chapter 6.

The same experimental program also revealed the engineering requirements for reliable cross-joint comparison. The early response-comparison studies showed that correlation-based interpretation depends on repeatable excitation, comparable sensor placement, stable acquisition timing, and the possibility of repeated excitation with averaging. In [14] and [15], this led to practical synchronization of excitation start with the acquisition frame and to repeated measurement workflows. However, these solutions remained tied to specific experimental configurations and did not yet provide a generalized synchronization concept applicable to distributed digital sensing nodes, long cable runs, timing drift, or temperature-dependent acquisition instability.

The synchronization-related publications [31–33] advanced this engineering requirement further. The study on thermal stability of a multi-channel precise time-tagging system [31], the study on multi-channel synchronization for picosecond time-tagging [32], and the study on

compensation of time-interval accuracy error [33] investigated timing stability, channel synchronization, and compensation of clock-related errors. In this Thesis, these results are used to support the cross-node sample synchronization (CNSS) concept described in Chapters 2 and 3. CNSS generalizes the synchronization requirement from start-of-frame alignment toward continuous sample-level consistency, which is required for waveform-level near/far comparison, time-reversal replay, and pointwise RCR evaluation in Chapter 5.

The time-reversal component of the framework evolved from earlier study on controlled replay and focusing. The study on nonlinear land-mine detection using wide-bandwidth time-reversal techniques [27] is not treated in this Thesis as a structural-joint diagnostic validation case. Instead, it provides methodological background for controlled time-reversed replay, focusing, and multi-emitter excitation. This experience is adapted in Chapter 2 for the formulation of multidimensional time-reversal impact focusing (MTRIF), where spatially distributed actuators are used to synthesize an axis-specific virtual impact at the near-sensor location.

The granted patent on non-destructive testing of building structures complements the scientific publications by documenting the system-level concept of integrated structural assessment. In the context of this Thesis, it supports the practical implementation perspective of the hardware–software framework described in Chapter 3 and the overall integration logic introduced in Chapter 1.

Together, the appended publications document the transition from localized response comparison toward a synchronized multidimensional diagnostic methodology integrating MTRIF, AMR, CNSS, and multiaxial coherence evaluation into a unified structural-joint assessment framework.

CHAPTER 2. METHODOLOGICAL SCOPE AND PREREQUISITES

2.1. Measured Quantities and Scale Treatment

The measured quantities are linear accelerations expressed in m/s². In this methodology, three linear-acceleration components are recorded on the near side and matched with three corresponding components on the far side to form three AMR pairs.

Sensor outputs are acquired as 16-bit digital values. Conversion to SI units is not required for the proposed diagnostic metrics, since the evaluation is based on normalized waveform comparison. Near and far signals forming each AMR pair are synchronized and normalized prior to RCR computation. Consequently, RCR and MCCM are treated as scale-independent coherence metrics derived from normalized acceleration data rather than absolute-amplitude measures.

The time axis in all plots is presented in milliseconds, while synchronization and signal comparisons are executed within the reconstructed common master clock domain.

2.2. Experimental Objects

Methodological validation was performed on structural joints encompassing various materials, connection types, and degradation scenarios. The research program included both timber and steel joints.

The experimental objects served two functions:

- supporting the development of individual methodological components reported in the appended publications [12–15];
- providing a baseline case for the final validation of the integrated framework.

Consistent with the Thesis format, the final methodology is validated on a baseline structural joint, while earlier experimental objects provide complementary evidence for specific components. Intermediate validation cases did not always employ the full integrated configuration but were essential for developing the underlying framework.

2.3. Sensor Configuration and Positioning Requirements

The measurement setup employs 3DOF accelerometers mounted on opposite sides of the structural joint (Fig. 2.1). Each sensor acquires three orthogonal linear-acceleration components – X, Y, Z. Matching these near-side components $X_{Near}, Y_{Near}, Z_{Near}$with the corresponding far-side axes $X_{Far}, Y_{Far}, Z_{Far}$ forms three AMR pairs.

This configuration enables the implementation of MTRIF by defining the near-sensor location as the virtual impact point. The resulting synchronized data provide the basis for per-axis RCR estimation and final MCCM fusion. The near sensor captures the reference excitation state, while the far sensor records the response transmitted through the joint interface.

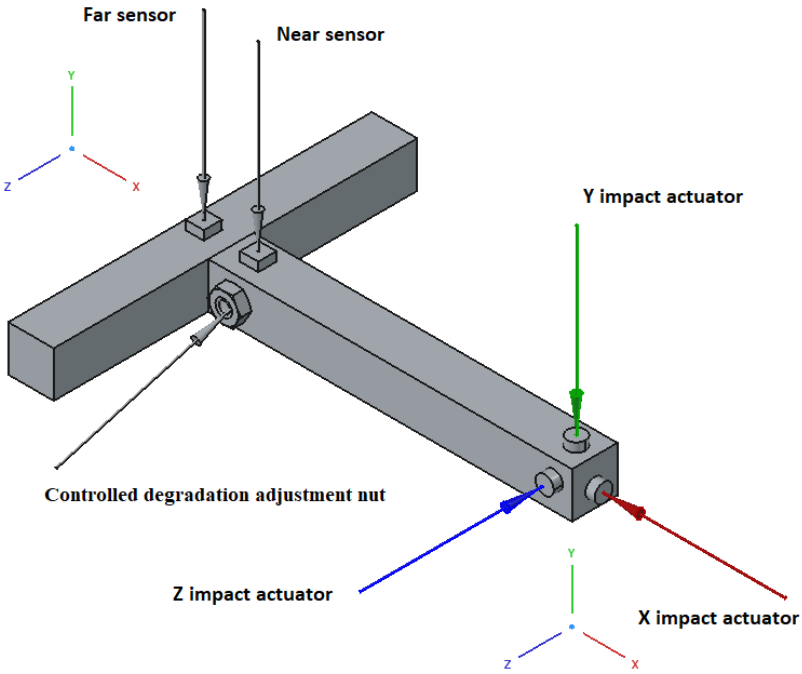


Fig. 2.1. Minimum sensor configuration and measurement geometry.

2.3.1. Virtual Coaxial Alignment Requirement

This requirement, termed virtual coaxial alignment, ensures that the matched axes of the near and far sensors are geometrically collinear and directionally consistent (Fig. 2.1). For valid AMR formation, alignment must be maintained between the corresponding linear-acceleration axes X, Y, Z of the two sensors.

In this framework, the near sensor is placed on the virtual impact side established by MTRIF, while the far sensor captures the response transmitted through the joint. In baseline implementation, alignment was achieved through precise physical mounting (detailed in Chapter 4). While residual misalignment could be corrected via coordinate frame transformation, this approach is treated as an extension and is discussed only in Chapter 7.

2.3.2. Effect on Waveform Comparability (RCR)

Waveform comparability within an AMR pair requires the spacing between near and far measurement points along a matched axis to be less than one-quarter of the shortest relevant wavelength $\lambda/4$. Violation of this condition increases phase mismatch, thereby reducing the reliability of pointwise coherence evaluation and the robustness of the RCR estimate (Section 2.9).

Figure 2.2 illustrates this effect for three normalized spacing conditions: 0, $\lambda/4$, and $\lambda/3$. As spacing increases, waveform overlap decreases, causing a corresponding drop in RCR. In the illustrated case, the $\lambda/4$ condition retains over 50 % of the reference metric level, whereas the $\lambda/3$ condition reduces it by more than a factor of two relative to the zero-shift baseline. This reduction represents a critical loss of diagnostic sensitivity for the RCR methodology.

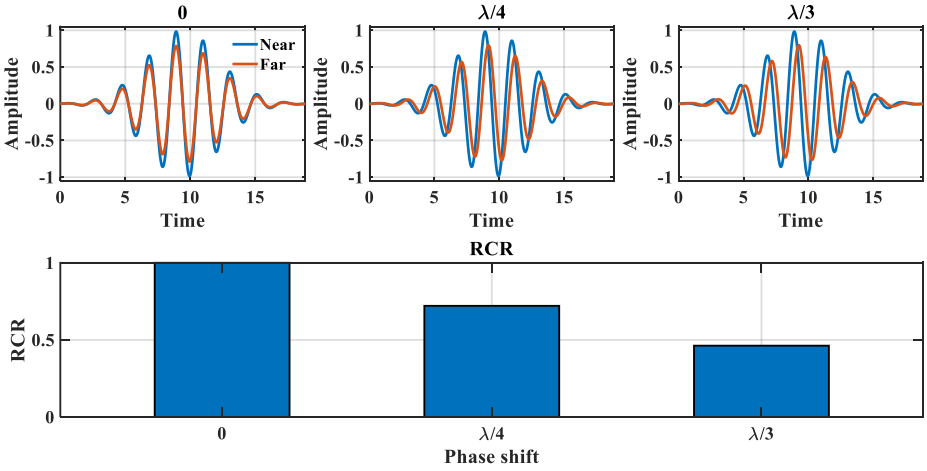


Fig. 2.2. Effect of phase shift on RCR.

2.3.3. Effect on Time-Reversal Defocusing

The λ/4 criterion also governs the spatial extent of the focal spot produced by MTRIF. Focused energy remains concentrated within a region of approximately λ/4 around the near-sensor location. If the far sensor is positioned beyond this focal region, it records a defocused, lower-amplitude signal that does not represent the intended virtual impact response.

The λ/4 condition is therefore critical for maintaining the physical validity of the near/far comparison (Fig. 2.3). While the near sensor captures the reference focused state, the far sensor must remain within the focal zone to record the corresponding transmitted response. Exceeding this spacing threshold leads to a loss of both RCR robustness and physical representativeness of the AMR pairs.

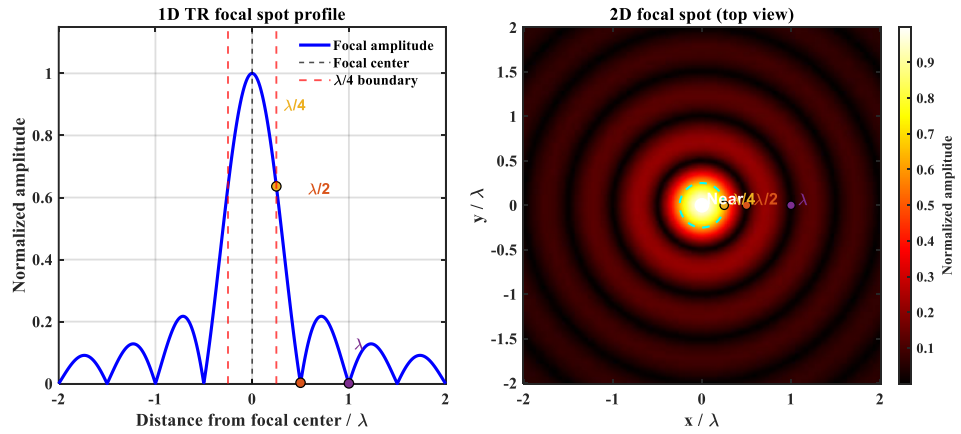


Fig. 2.3. TR focal spot and defocusing with increasing distance from the focus.

2.3.4. Practical Bandwidth Criterion for Sensor Spacing

The maximum permissible distance between near and far measurement points is constrained by the highest usable frequency $f_{\max}$ in the signal. This frequency is determined by the Nyquist limit, actuator bandwidth, structural dynamics, and the system noise floor.

In this study, signal components remain observable up to 9 kHz (Fig. 2.4). The maximum admissible spacing $d_{\max}$ is defined by the quarter-wavelength criterion:

$$d_{\max} \approx \frac{\lambda_{\min}}{4} = \frac{c_p(f_{\max})}{4 f_{\max}} \tag{2.1}$$

Variables in Eq. (2.1) are defined as follows: $\lambda_{\min}$ is the minimum wavelength at $f_{\max}$; $c_p(f_{\max})$ is the flexural-wave phase velocity; and $f_{\max}$ is the upper frequency limit.

For the HEA 100 steel beam, the phase velocity at 9 kHz is 2.7–3.4 km/s, resulting in a $\lambda/4$ limit of 75–96 mm. The experimental near/far spacing was approximately 30 mm (Fig. 4.2 (a)), which satisfies the criterion without additional bandwidth restrictions. If larger spacing is required, $f_{\max}$ must be reduced via zero-phase filtering to maintain wavelength compatibility with the sensor positions.

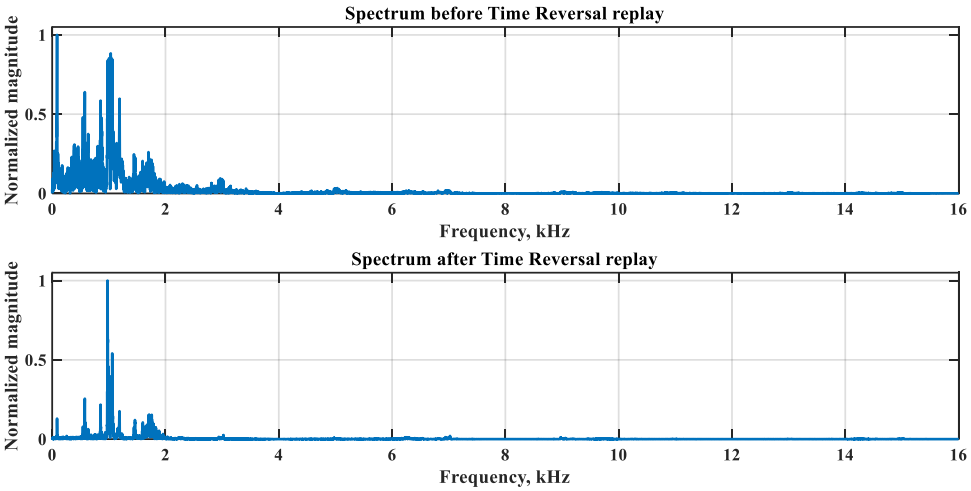


Fig. 2.4. Measured response spectra before and after time-reversal replay.

2.4. Actuator Configuration and Positioning Requirements

The actuator configuration must provide diverse excitation paths to facilitate multiaxial activation at the target region. Ideally, actuators are arranged to excite the principal directions of structural response independently. This independence is enhanced by increasing the number of actuators or introducing controlled asymmetry through off-center placement to stimulate complex wavefields.

The MTRIF framework does not require pure single-axis excitation at individual actuator locations. Instead, it relies on distinct transfer paths to ensure that time-reversed wavefields converge at the near-sensor location, producing a focused multiaxial response. This multidimensional focus is essential for stimulating all three orthogonal axes represented in the AMR pairs.

In this study, a three-actuator configuration was implemented as a baseline solution. This arrangement facilitates both axis-selective sequential replay and multicomponent response activation. The role of the actuator configuration is to provide a sufficient basis for multidimensional focusing at the near location, enabling robust RCR estimation and MCCM fusion. The practical realization of this three-actuator setup is detailed in Fig. 4.2 (b).

2.5. Degradation Emulation

Progressive joint degradation is defined in this Thesis as a controlled reduction or modification of the mechanical coupling and stiffness of the investigated connection. In the appended publications, degradation-sensitive behavior was investigated under different structural and material scenarios, including direction-dependent response changes, selective fastener removal, bolt-torque variation, and measurements performed under varying static loading conditions. These studies provided complementary evidence that joint condition changes may affect different response axes in different ways.

For the integrated framework developed in this Thesis, degradation emulation is used to generate repeatable structural states with progressively altered transmission properties across the joint. The purpose of this sequence is not to reproduce every possible real damage mechanism, but to provide controlled joint-integrity states for evaluating whether the MTRIF–AMR diagnostic cycle and multiaxial near/far comparison remain sensitive to progressive changes in joint condition.

In the baseline validation experiment, this concept was implemented by controlled reduction of bolt tightening torque (Fig. 4.2 (c)). The specific degradation sequence is detailed in Subsection 4.1.3 and Chapter 4.

2.6. Time-Reversal Impact Focusing Principles

Time reversal (TR) is a wavefield refocusing technique grounded in the principle of reciprocity. Following [18], time reversal is equivalent to phase conjugation in the frequency domain. For a propagated signal,

$$Y(\omega) = H(\omega)S(\omega), \tag{2.2}$$

time reversal gives

$$Y_{TR}(\omega) = Y^{*}(\omega), \tag{2.3}$$

and the refocused field becomes

$$Z(\omega) = H(\omega)\, Y^{*}(\omega) = H(\omega)\, H^{*}(\omega)\, S^{*}(\omega) = |H(\omega)|^{2}\, S^{*}(\omega), \tag{2.4}$$

where Y(ω) is the received signal spectrum, S(ω) is the excitation spectrum, H(ω) is the transfer function of the structure, Z(ω) is the refocused field, the superscript (*) denotes complex conjugation, and ω represents angular frequency.

Within this framework, TR serves as a mechanism for the virtual relocation of excitation from a physical actuator to a remote target position. By replaying time-reversed responses, injected energy is spatially localized and focused at the target location.

For broadband mechanical impacts, the structure selectively transmits frequency components compatible with its dynamic properties. Re-emitting the time-reversed response from the actuator location causes wave fronts to converge at the original recording point, recreating a focused excitation. TR therefore functions as both a virtual relocation mechanism and a physically selective focusing process.

The basic TR procedure consists of four steps:

1) emission of a broadband impulse into the structure via an actuator (Fig. 2.5 a));
2) acquisition of the response at the target sensor position (Fig. 2.5 b));
3) re-emission of the time-reversed acquired signal (Fig. 2.5 c));
4) acquisition of the response at the target sensor position (Fig. 2.5 d)).

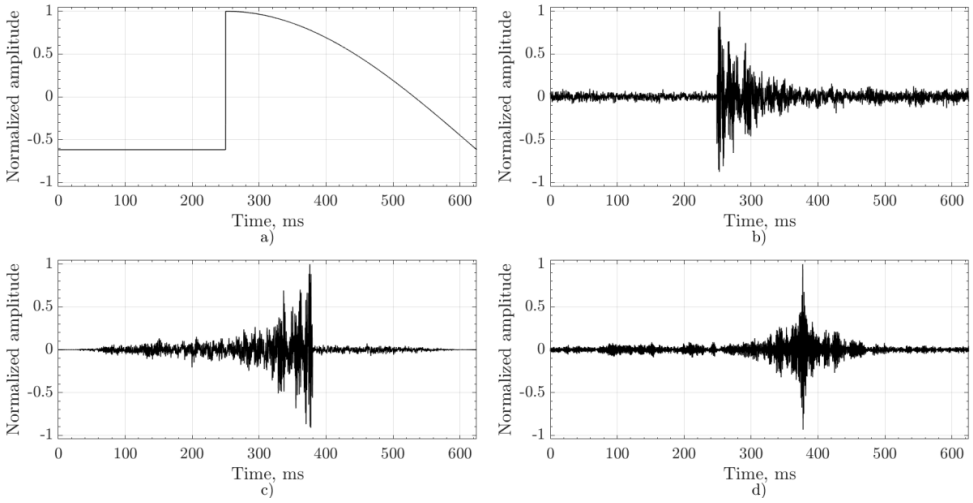


Fig. 2.5. Four-step time-reversal procedure in one dimension.

A representative practical application relevant to this principle was implemented by the author in an earlier study on buried land-mine detection using time-reversal focusing with multiple emitters and a single receiver [27] (Fig. 2.6). In that application, coordinated replay from several actuators increased the focused energy at the target region and demonstrated that time-reversal focusing can remain effective even in strongly attenuative media. In the context of the present Thesis, this earlier result is important not as a direct structural-joint experiment but as a methodological precedent showing that coordinated multi-actuator replay can be used

to concentrate energy at a selected remote location. This principle forms the conceptual basis for the multidimensional extension introduced in the following section.



Fig. 2.6. Experimental time-reversal land-mine detection setup.

2.7. Multidimensional Time-Reversal Impact Focusing (MTRIF)

The MTRIF framework extends the TR principle from single-component focusing to simultaneous multiaxial excitation at the point of interest. The procedure is executed as follows.

1. A broadband pulse is emitted by the actuator oriented along the X direction (Fig. 2.7 a)), and the collinear X-component of the response is recorded at the near sensor (Fig. 2.7 b)).
2. A broadband pulse is emitted by the actuator oriented along the Y direction (Fig. 2.7 e)), and the collinear Y-component of the response is recorded at the near sensor (Fig. 2.7 g)).
3. A broadband pulse is emitted by the actuator oriented along the Z direction (Fig. 2.7 i)), and the collinear Z-component of the response is recorded at the near sensor (Fig. 2.7 l)).
4. MTRIF replay preparation: The captured collinear X, Y, and Z components are normalized and time-reversed. These waveforms are assigned as replay signals for their corresponding actuators.
5. Simultaneous replay: The three time-reversed signals are emitted simultaneously, each through the same actuator used during the characterization step. This synchronized emission generates a simultaneous triaxial focused response at the near-sensor position (Figs. 2.8 e), 2.8 k), and 2.8 q)).

To improve repeatability and suppress uncorrelated noise, each excitation signal in the MTRIF workflow was emitted multiple times. The corresponding responses recorded at the receiving sensor side were averaged before being used for replay preparation or subsequent metric evaluation.

Although only the collinear components are used to synthesize the MTRIF replay signals, the full triaxial response is recorded at each characterization step to monitor the system's behavior. As shown in Fig. 2.7, structural coupling and modal mixing mean that the peak response does not always occur in the axis nominally collinear with the actuator. This can be observed for the X, Y, and Z-direction excitation cases in Figs. 2.7 b)–d), 2.7 f)–h), and 2.7 j)–l), respectively.

For verification only, the prepared time-reversed signals were also replayed sequentially (Figs. 2.8 a)–d), 2.8 g)–j), and 2.8 m)–p)). This step is not part of the final MTRIF excitation procedure; it is used to confirm that time-reversed replay increases the contrast of the intended target components at the POI.

During simultaneous replay, the transmitted response is also recorded at the far sensor (Figs. 2.8 (f), 2.8 (l), and 2.8 (r)). This response is not used to construct the MTRIF excitation itself, but it is later used in AMR, RCR, and MCCM evaluation. Thus, the procedure establishes the repeatable and synchronized triaxial excitation condition required for the proposed diagnostic framework.

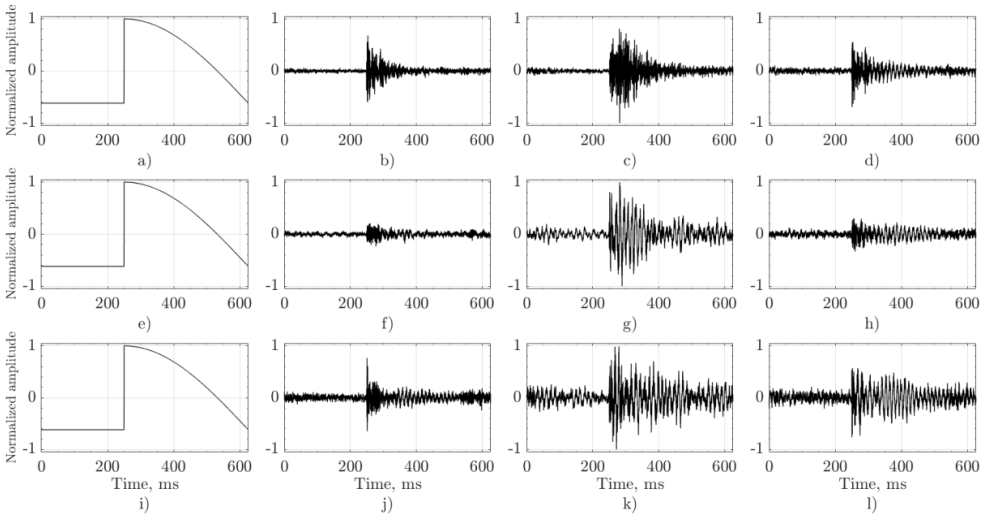


Fig. 2.7. Originally emitted signals and selected directional response signals for replay preparation.

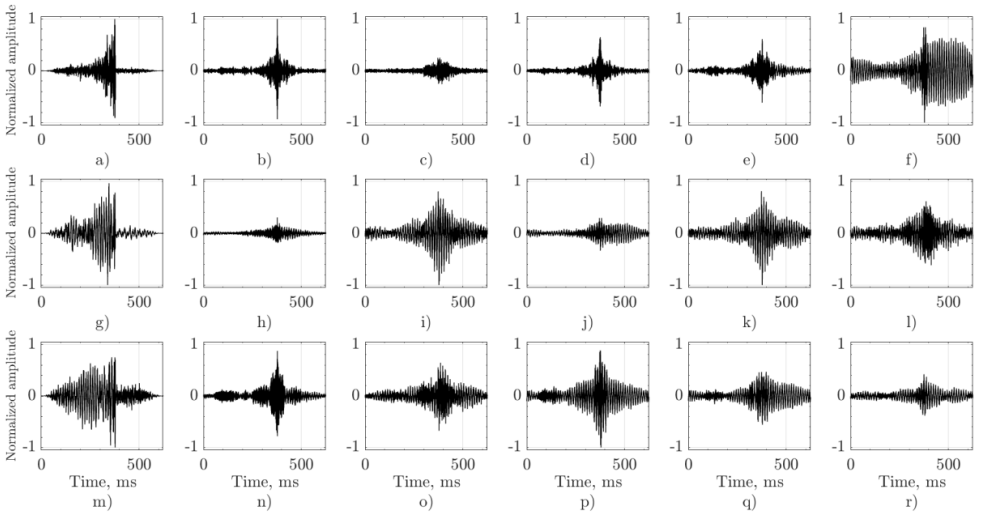


Fig. 2.8. Multiaxial response to time-reversed replay.

2.8. Time-Domain Coherence Prerequisite and CNSS Rationale

Both time-reversal focusing and RCR-based comparison require continuous sample-level alignment across all channels. Start-time synchronization alone is insufficient because independent clock domains diverge due to static offset and temperature-dependent drift. This divergence degrades the time consistency required for MTRIF replay and pointwise comparison.

To maintain signal comparability, the accumulated timing inconsistency $\Delta t_{\max}$ must satisfy the quarter-period criterion relative to the highest retained frequency $f_{\max}$:

$$\Delta t_{\max} < \frac{1}{4 f_{\max}} \tag{2.5}$$

The variables in Eq. (2.5) are the maximum admissible accumulated timing error $\Delta t_{\max}$ and the highest usable frequency $f_{\max}$. For a 32 kHz sampling rate, the Nyquist frequency is 16 kHz period $T = 62.5$ μs, yielding a $\Delta t_{\max}$ limit of 15.6 μs. A typical oscillator mismatch of 30 ppm over 10 s produces 300 μs of error, exceeding the acceptable threshold [31, 33].

CNSS preserves a common time reference across independently clocked nodes. Figure 2.9 illustrates: (a) the signal in the master clock domain; (b) the signal in the local sensor clock domain under drift; and (c) the signal reconstructed via marker-based resampling. Recorded markers serve as timing observables to estimate mismatch and restore sample-level alignment [32, 33]. Although deviations in Fig. 2.9 are exaggerated for clarity, uncorrected real-world drift is sufficient to degrade phase consistency and RCR evaluation.

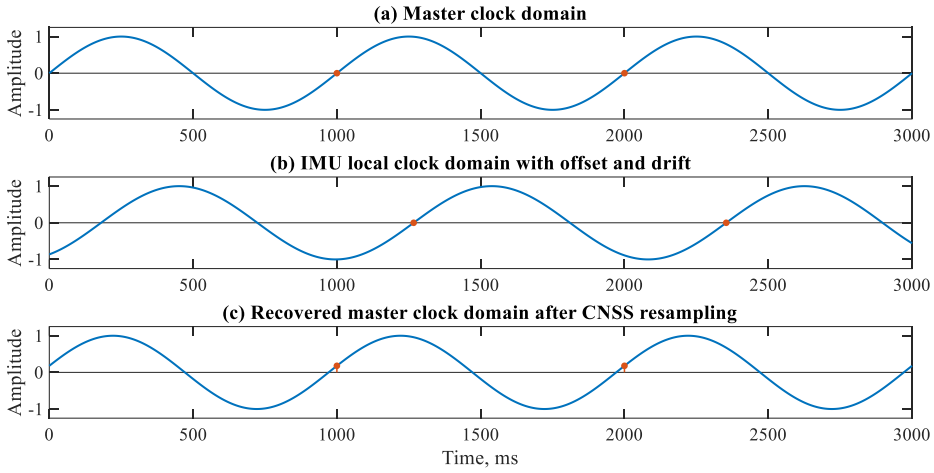


Fig. 2.9. Illustration of clock offset, drift, and marker-based recovery via CNSS.

2.9. Response Coherence Ratio (RCR)

Because the proposed methodology evaluates three AMR pairs formed by matched linear-acceleration components measured along corresponding axes on the near and far sides of the joint, the key challenge was to select an appropriate per-axis coherence metric [12–14]. The selected metric should be:

- invariant to absolute amplitude;
- sensitive to waveform shape and relative amplitude within corresponding AMR;
- robust to low-energy or noisy AMR pairs.

During the development of the methodology, several candidates were considered:

- normalized cross-correlation RMS (NCCR);
- Pearson correlation coefficient;
- cosine similarity;
- response coherence ratio (RCR).

Table 2.1

Qualitative comparison of candidate per-axis similarity metrics used during metric selection

Metric	Amplitude invariance	Shape sensitivity	Noise robustness	Notes
NCCR	✓	✓	✗ Poor on noisy axes	Fails on low-signal channels
Pearson correlation	✓	✓	✗ Poor on noisy axes	Classical but unstable at low SNR
Cosine similarity	✓	✗ Poor	✗ Poor on noisy axes	Unstable under partial match
RCR	✓	✓	✓ Robust	Best suited for 3DOF MCCM

A comparative evaluation of the candidate per-axis similarity metrics is presented in Table 2.1. On the basis of this evaluation, RCR was selected as the final per-axis metric because it offers the best balance among shape sensitivity, amplitude invariance, noise robustness, and practical repeatability within the AMR cross-joint evaluation framework [12–14]. Specifically, the peak-to-RMS formulation of RCR (detailed in Section 5.1) naturally attenuates noisy or weakly activated channels because random noise produces a low peak-to-RMS ratio, whereas a coherent waveform match produces a pronounced peak in the pointwise product signal. This self-weighting property makes RCR better suited than Pearson correlation or cosine similarity for applications where individual AMR pairs may have substantially different signal-to-noise ratios. A quantitative comparison of all four candidate metrics on the same baseline dataset is documented in the appended publications [12, 14].

2.10. Multiaxial Component Coherence Metric (MCCM)

The MCCM is the fused scalar indicator of joint condition within the proposed framework [12, 14, 15]. It consolidates the three per-axis RCR values derived from the linear-acceleration AMR pairs into a single scalar metric. This fusion reduces axis-dependent dispersion and enhances the interpretability of the joint-condition assessment. The Euclidean-norm formulation was selected over alternative fusion strategies (weighted sum, geometric mean, or minimum-value approaches) because it preserves the contribution of all three axes without requiring prior knowledge of axis-specific sensitivity or weighting coefficients. The mathematical procedure for MCCM computation is detailed in Section 5.2.

CHAPTER 3. HARDWARE–SOFTWARE PLATFORM FOR DATA ACQUISITION

3.1. Purpose and Scope of the Platform

The proposed methodology requires a dedicated hardware–software platform providing the following capabilities:

- synchronized multi-actuator excitation;
- multi-channel 6DOF sensing;
- high noise immunity for remotely placed sensors;
- high-speed bidirectional data transfer between the acquisition hardware and the host computer;
- precise long-term time-domain synchronization between actuators and sensors.

Together, these requirements define the minimal functional platform structure shown in Fig. 3.1 [14, 27, 31–33]. Its detailed architecture and subsystem organization are described in the following sections.

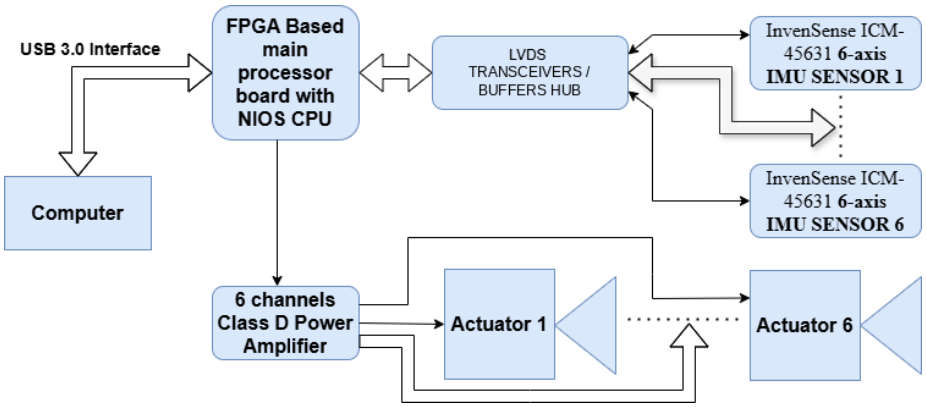


Fig. 3.1. Hardware–software platform block diagram.

3.2. System Overview and Core Architecture

The core architecture is centered on an FPGA-based main processor board (Intel Cyclone IV EP4CE22), which provides the acquisition and control functions required by the platform (Fig. 3.1), including:

- timing control in the platform master clock domain;
- excitation waveform generation and control;
- acquisition and handling of SPI data streams from distributed IMU sensors;
- frame synchronization marker generation, injection, and capture;
- data framing and packaging for recording and transfer.

Sensor data are transferred through a hub of LVDS transceivers and buffers that extends the digital SPI sensor interface over long cable runs to the FPGA, providing high noise immunity and enabling remote sensor placement. Actuators are driven by a custom six-channel Class D power amplifier controlled by the FPGA unit. Communication with the host computer is provided through a USB 3.0 interface for platform configuration, measurement control, and high-speed bidirectional dataset transfer.

3.3. Excitation Subsystem

The excitation subsystem delivers controlled mechanical input to the structure. It consists of a custom six-channel Class D power stage driving up to six vibration actuators. The amplifier is controlled via an I²S digital audio bus, enabling real-time waveform streaming from the FPGA without the need for extensive on-chip memory. The Class D topology ensures high efficiency and low heat dissipation during multi-channel operation.

The actuators are resonance-based vibration speakers attached directly to the structural member (Fig. 3.2). These devices inject vibrations into the surface, using the structure itself as the radiating medium. This configuration ensures efficient mechanical coupling and compact mounting suitable for MTRIF excitation.

In the current implementation, the effective bandwidth is limited by the sensor sampling rates. For the accelerometer channels, the usable upper frequency limit is approximately 16 kHz.



Fig. 3.2. Resonance speaker used as an actuator.

3.4. Sensing, Acquisition, and Noise-Robust Data Transfer

The platform supports up to six 6DOF IMU nodes, utilizing the ICM-45631 as the primary sensor. Although the hardware provides full 6DOF acquisition (three translational and three rotational channels), the current study focuses exclusively on the three linear-acceleration channels to satisfy the 3DOF methodology requirements. The implementation uses a 32 kHz sampling rate for the accelerometer data and 8 kHz for the gyroscope data.

Data acquisition is executed via SPI and transmitted to the FPGA through LVDS extenders, supporting cable lengths up to 100 m. This configuration ensures high noise immunity for remote sensor deployment. The FPGA performs framing, buffering, and packaging of the

multichannel data stream for host computer transfer. The sensor-side architecture is shown in Fig. 3.1.

3.5. Time-Reference Support and CNSS Observables

The independent clock domains of distributed sensor nodes and the master excitation controller necessitate active timing compensation. Even with a common start event, local sensor time bases diverge from the master clock due to static offset and thermal drift, violating the requirements for MTRIF and RCR analysis [31–33].

To quantify this divergence, the platform injects periodic synchronization markers into each acquisition stream. These markers function as timing observables, captured synchronously with sensor data to estimate accumulated mismatch without modifying the local clocking of the remote nodes. During signal processing, these observables are used to reconstruct all channels into a common master clock domain, ensuring the phase consistency required for valid pointwise waveform comparison of AMR pairs.

The timing studies reported in [31–33] demonstrated picosecond-level synchronization and time-interval compensation capabilities. In the present platform, these results are used as the methodological and engineering basis for CNSS; however, such accuracy is not required for the acceleration-sensing channel considered here. The accelerometer data are acquired at 32 kHz, corresponding to a sampling interval of 31.25 μs. For the retained upper frequency of 16 kHz, the quarter-period timing criterion corresponds to a maximum admissible timing deviation of 15.6 μs, equivalent to approximately 9.0 μs RMS under a uniform-error assumption. A single reconstructed measurement therefore remains close to the admissible timing limit. To obtain a robust timing margin, repeated marker-aligned measurements are averaged, reducing the random timing component in proportion to $1/\sqrt{N}$. With four repeated measurements, the effective uncertainty is reduced to approximately 4.5 μs RMS, while the eight repeated measurements used in this study reduce it further to approximately 3.2 μs RMS. Thus, after marker-based reconstruction and averaging, the timing requirement for the present acceleration-sensing channel is satisfied with a clear margin.

3.6. Control Software and User Interface

A dedicated host-PC software suite was developed as part of this study to serve as the operational front end for the platform. The software integrates experiment control, live monitoring, and dataset management within a unified environment, ensuring seamless interaction between the user and the hardware. Key functions of the developed software include:

- excitation management: waveform preparation and multi-channel assignment;
- hardware control: configuration and execution of acquisition cycles;
- data processing: marker-based resynchronization, frame alignment, and real-time visualization;
- iterative workflow: replay signal preparation for MTRIF operation;
- storage: multi-channel data recording and export for post-processing.

This integrated approach enables precise experimental control and efficient data handling, directly supporting the methodology described in this Thesis.

3.7. Key Specifications of the Platform

The technical characteristics of the platform are summarized in Table 3.1. These parameters define the operational limits for sensing, excitation, synchronization, and data transfer. The timing principles and accuracy margin of the CNSS approach are discussed in Section 3.5 and supported by the studies reported in [31–33].

Table 3.1

Key platform specifications

Parameter	Specification
Sensor nodes	Up to 6 × 6DOF IMU (ICM-45631)
Linear acceleration ODR	32 kHz (used for 3DOF methodology)
Angular velocity ODR	8 kHz (hardware supported)
Effective bandwidth	Sensor-limited: ~16 kHz (acceleration)
Accelerometer range	Programmable: ±2g to ±16g
Accelerometer noise density	90 μg/√Hz
Excitation channels	6 × Class D (up to 100 W peak/channel)
Vibration actuators	6 × Resonance vibrators (25 W rated)
Remote sensor link	SPI over LVDS (up to 100 m)
Host interface	USB 3.0

CHAPTER 4. DATA COLLECTION

4.1. Baseline Object and Joint Configuration

The baseline validation employed a structural steel stand consisting of two S355 (HEA 100) beams connected by a semi-rigid bolted joint. The connection was secured with a single M16 bolt (strength class 8.8). This configuration was chosen to ensure a repeatable joint condition under progressive stiffness variation and multiaxial measurements. The experimental setup is illustrated in Fig. 4.1.



Fig. 4.1. Baseline steel beam stand.



Fig. 4.2. Baseline experimental arrangement.

4.1.1. Sensor Placement

Two 3DOF sensors were mounted on opposite sides of the joint, 30 mm from the centerline on separate beam elements (Fig. 4.2 (a)). The near sensor defines the virtual impact location for MTRIF, while the far sensor captures the transmitted wavefield.

Sensor axes $X, Y,$ and Z were physically aligned during installation to establish the three AMR pairs required for analysis. This placement ensures the virtual coaxial alignment necessary for pointwise signal comparison without additional coordinate transformations.

4.1.2. Actuator Placement

Three resonance actuators were mounted on the near-side beam to excite the $X, Y,$ and $Z-$ axes (Fig. 4.2 (b)). The actuators were spatially distributed to provide the transfer paths required for MTRIF. This configuration ensures multidimensional activation at the near-sensor location (virtual impact point) without placing physical transmitters directly at the POI.

4.1.3. Degradation Method

In the baseline validation experiment, progressive joint degradation was emulated by a controlled reduction in the bolt-tightening torque using a torque wrench (Fig. 4.2 (c)). This procedure was selected as a repeatable and reversible means of modifying the mechanical coupling and stiffness of the bolted joint without altering the sensor or actuator configuration.

The torque was reduced from 175 N·m to 0 N·m across eight predefined degradation stages. Within this experiment, the torque sequence is treated as a controlled set of joint-integrity states rather than a comprehensive representation of all possible real damage mechanisms. Its purpose is to provide a consistent sequence of altered transmission properties to demonstrate the MTRIF–AMR diagnostic cycle and to evaluate the sensitivity of the axis-matched near/far responses to progressive joint-condition changes.

4.2. Measurement Steps

The experimental process was structured as a repeated measurement–degradation cycle. To ensure consistency across degradation states, the same MTRIF procedure was applied at each torque level without modifying the sensor or actuator placement.

The workflow was executed as follows.

1. START: The joint was set to the baseline condition, corresponding to the fully tightened state at 175 N·m.
2. MEASURE: The complete MTRIF procedure described in Section 2.7 was performed for the current joint state.
3. RECORD: The triaxial near and far responses obtained during the simultaneous replay phase were stored for the current state.
4. DEGRADE: The joint stiffness was reduced by decreasing the tightening torque of the M16 bolt to the next predefined level.
5. GOTO MEASURE: The measurement–degradation cycle was repeated until the fully loosened state was recorded.

The degradation sequence consisted of eight torque levels.

Stage 1: 175 N·m, baseline tightened condition.

Stages 2–8: 150 N·m, 125 N·m, 100 N·m, 75 N·m, 50 N·m, 25 N·m, 0 N·m, fully loosened condition.

Completing this loop through all eight stages yielded the final response dataset. For each stage, three linear acceleration components were recorded at both the near and far sensors during the simultaneous MTRIF replay.

The complete measurement–degradation sequence was repeated five times without changing the sensor and actuator configuration. Each repetition covered the same eight torque levels from 175 N·m to 0 N·m. Consequently, the repeated dataset contains:

3 channels × 2 sensors × 8 stages × 5 repetitions = 240 response signals, corresponding to:

3 AMR pairs × 8 stages × 5 repetitions = 120 AMR pairs.

This repeated dataset enables both degradation-trend evaluation and repeatability analysis through standard deviations of the per-axis RCR values and the fused MCCM.

CHAPTER 5. SIGNAL PROCESSING AND METRIC EVALUATION

This chapter details the computational procedures for transforming the synchronized near/far sensor responses into diagnostic indicators. While Chapter 2 established the conceptual definitions and methodological rationale for the AMR, RCR, and MCCM components, the present chapter specifies the complete processing algorithms as applied to the experimental dataset. The workflow is applied independently to each of the three linear-acceleration AMR pairs: $\mathrm{AMR_x}, \mathrm{AMR_y}, \text{and } \mathrm{AMR_z}$.

In the proposed methodology, RCR and MCCM provide the per-axis evaluation and multiaxial fusion layers of the diagnostic workflow. Their functional roles remain fixed within the proposed framework, while the specific computational implementation may be adapted depending on the sensing configuration, signal characteristics, and application constraints. The computational procedures presented below are used to quantify the degradation-sensitive response of the MTRIF–AMR framework; the primary scientific novelty lies in the integrated diagnostic methodology rather than in the specific computational formulations.

5.1. Per-Axis RCR Evaluation

- DC offset removal: Constant components are suppressed to eliminate gravity-related offsets:

$$\mathrm{s_{dc}} = \mathrm{s} - \bar{\mathrm{s}}. \tag{5.1}$$

- Normalization: Signals in the AMR pair are scaled by their common maximum absolute amplitude A:

$$\mathrm{s_n} = \mathrm{s_{dc}}/A. \tag{5.2}$$

- Band-pass filtering: Signals are restricted to the target frequency range:

$$\mathrm{s_{bpf}} = \mathrm{B}(\mathrm{s_n}). \tag{5.3}$$

- Pointwise multiplication: An intermediate product signal p is generated:

$$\mathrm{p} = \mathrm{s}_{\mathrm{Near}}^{\mathrm{bpf}} \cdot \mathrm{s}_{\mathrm{Far}}^{\mathrm{bpf}}. \tag{5.4}$$

- RCR extraction: The final scalar for the axis is the peak-to-RMS ratio of the product signal:

$$\mathrm{RCR} = \max|\mathrm{p}| \,/\mathrm{RMS}(\mathrm{p}). \tag{5.5}$$

The variables used in Eqs. (5.1)–(5.5) are:
s – the recorded signal; $\bar{\mathrm{s}}$ – the mean signal value; $\mathrm{s_{dc}}$ – the offset-corrected signal;
A – the normalization factor; $\mathrm{s_n}$ – the normalized signal; B – the band-pass operator; iss_{bpf} – the filtered signal; p – the pointwise product; and RMS – the root mean square operator.

All signals are processed in the reconstructed master clock domain.

5.2. MCCM Computation

After the per-axis RCR values are calculated for the X, Y, and Z AMR pairs, they are combined into the multiaxial component coherence metric (MCCM). In the present implementation, MCCM is computed as the Euclidean norm of the three per-axis RCR components:

$$MCCM = \sqrt{RCR_x^2 + RCR_y^2 + RCR_z^2}, \tag{5.6}$$

where RCR_x, RCR_y, and RCR_z are the response coherence ratio values obtained from the corresponding X, Y, and Z AMR pairs.

The computation is performed independently for each degradation stage and, in the repeated-measurement dataset, for each measurement cycle. Thus, every torque level is represented by one MCCM value per repetition.

CHAPTER 6. METRIC EVALUATION RESULTS

This chapter presents quantitative results from five repeated measurement–degradation cycles performed across eight torque levels. Joint degradation was emulated by reducing the tightening torque from 175 N·m to 0 N·m. The repeated dataset contained 240 response signals, corresponding to 120 AMR pairs. RCR was computed independently for each axis, torque level, and repetition, and the resulting values were fused into MCCM for each degradation state.

The repeated cycles allow the monotonic degradation trend, metric repeatability, and dispersion to be evaluated. The results are presented as per-axis RCR trends, fused MCCM behavior, and standard-deviation-based stability analysis.

6.1. Per-Axis RCR Repeatability Across Five Measurement Cycles

The per-axis RCR results are shown in Fig. 6.1. All values are normalized to the baseline condition of each repetition, corresponding to 175 N·m. In all cycles, the highest RCR values occur at the baseline condition, while progressive torque reduction causes a clear decrease in coherence across all three AMR pairs.

The repeated cycles show a reproducible degradation pattern, but the X, Y, and Z components differ in slope and dispersion. This reflects anisotropic wave transmission through the joint and direction-dependent sensitivity to bolt loosening. Therefore, single-axis interpretation remains vulnerable to axis-specific variability, whereas retaining all three RCR components provides a more complete representation of the joint condition.

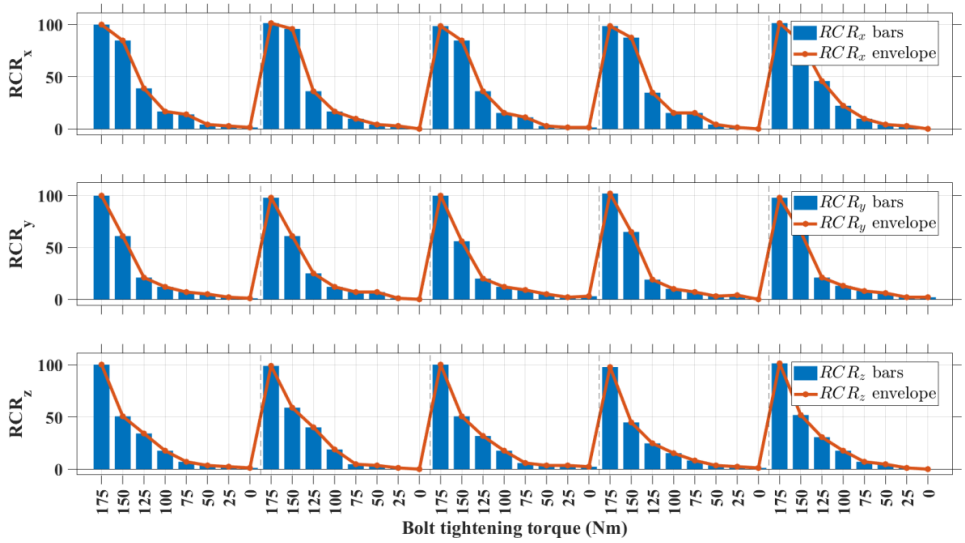


Fig. 6.1. Per-axis RCR values.

6.2. MCCM Repeatability and Degradation Trend

The fused MCCM results are shown in Fig. 6.2. All values are normalized to the initial baseline of each repetition, corresponding to 175 N·m. Compared with the individual RCR components, MCCM provides a more compact and interpretable degradation profile. In all five repeated measurement cycles, MCCM decreases consistently from the baseline condition toward the fully loosened 0 N·m condition.

The repeated MCCM trend confirms that the fused metric preserves the degradation-sensitive information contained in the three AMR pairs while reducing axis-dependent variability. The monotonic or near-monotonic decrease within each repetition supports the use of MCCM as the primary scalar indicator for joint-condition tracking. At the same time, the individual RCR components remain useful for directional interpretation and for identifying which response axes are most affected by the change in joint stiffness.

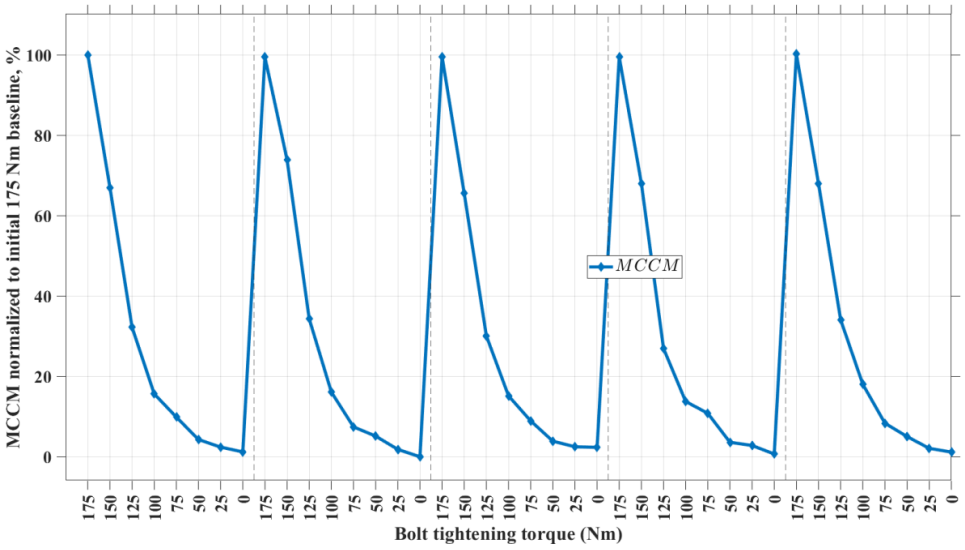


Fig. 6.2. MCCM values.

6.3. Dispersion Analysis of RCR and MCCM

The standard deviations of the per-axis RCR values across the five repetitions are shown in Fig. 6.3. The dispersion is low near the fully tightened baseline condition and increases as the tightening torque is reduced. This increase is especially pronounced at low torque levels, where the joint interface becomes mechanically less constrained and more sensitive to small variations in contact state, friction, and local boundary conditions.

The standard deviation of MCCM is shown in Fig. 6.4. Although the fused metric also exhibits increasing dispersion toward the loosened condition, its variability remains lower and more compact than the maximum dispersion observed among the individual RCR axes. This

confirms that the MCCM fusion procedure suppresses part of the axis-dependent variability while preserving the overall degradation trend.

A direct comparison between mean per-axis dispersion, maximum per-axis dispersion, and MCCM dispersion is presented in Fig. 6.5. The fused MCCM standard deviation remains below the maximum individual-axis standard deviation over the degradation sequence, demonstrating that multiaxial fusion improves the stability of the diagnostic indicator. The increase in dispersion at low torque levels should not be interpreted as a failure of the method; rather, it reflects the physically unstable contact condition of a loosened bolted joint, where small changes in interface state can produce larger changes in the measured dynamic response.

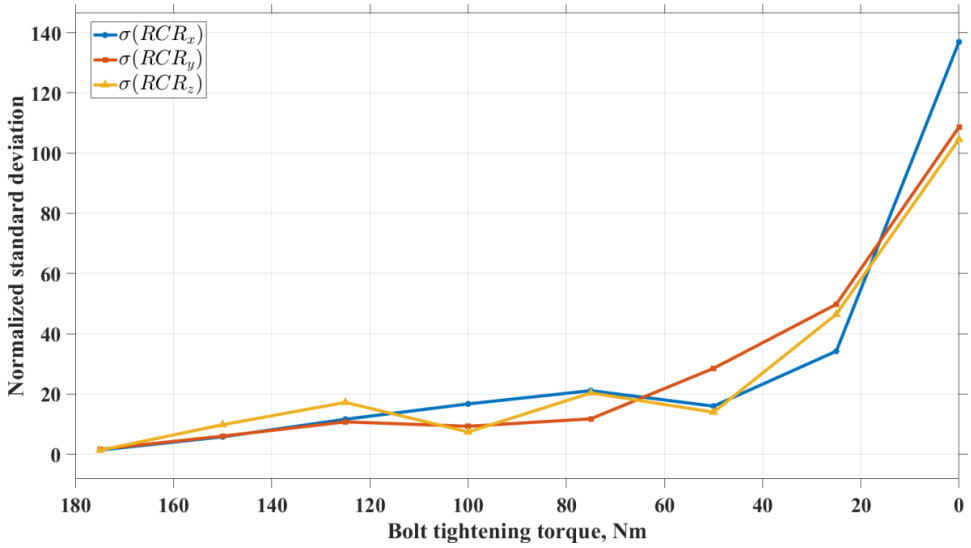


Fig. 6.3. Per-axis RCR standard deviation.

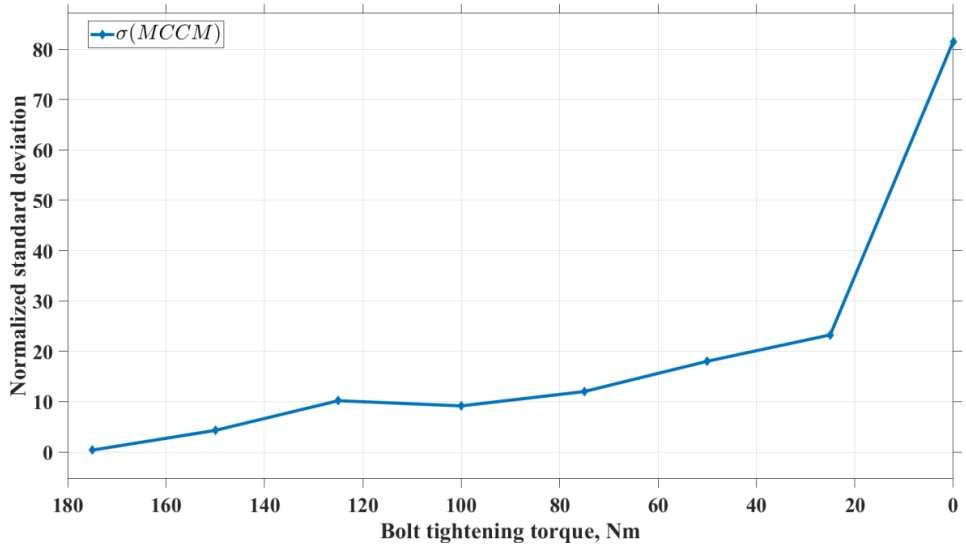


Fig. 6.4. MCCM standard deviation.

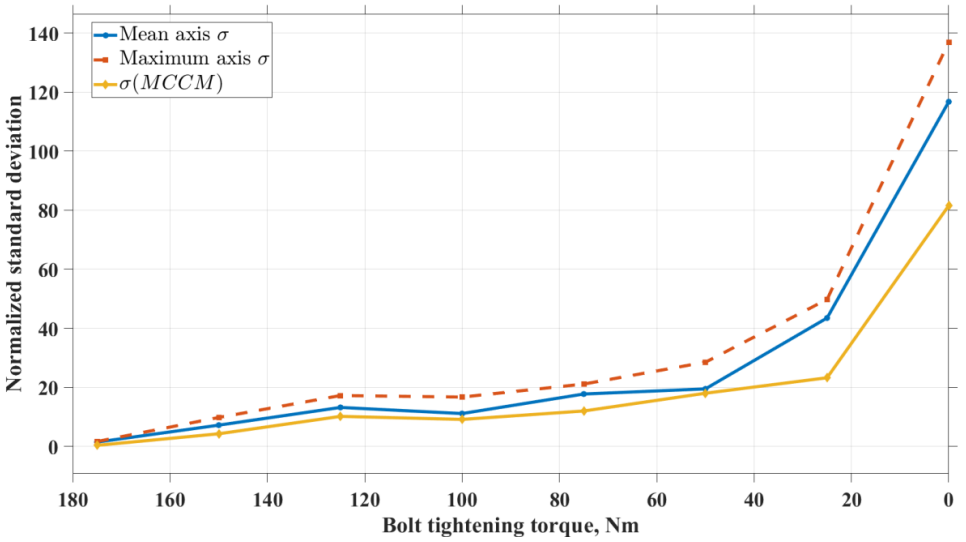


Fig. 6.5. RCR and MCCM dispersion comparison.

CHAPTER 7. FINAL REMARKS

This chapter summarizes the core findings, provides practical implementation guidelines, and outlines future development paths for the diagnostic framework.

7.1. Main Conclusions

This Thesis developed and experimentally validated a multidimensional framework for the non-destructive assessment of structural joints. The results support the core premise that reliable joint diagnostics benefit substantially from a multidimensional approach encompassing both controlled excitation and multiaxial response evaluation.

1. 3DOF sensing and AMR: The results confirm that the three linear-acceleration AMR pairs contain diagnostically relevant coherence information. In the baseline dataset, degradation-related variation was observable across all three pairs, providing a comprehensive view of joint integrity.
2. MTRIF implementation: The principal contribution is the formulation of MTRIF, which synthesizes a multiaxial excitation condition at the near-sensor location. This enhances the observability of degradation-related changes across multiple response components compared with conventional single-axis excitation.
3. Metric performance: At the per-axis level, the RCR effectively quantifies waveform similarity between near and far responses. At the fused level, the MCCM provides a stable and interpretable indicator, suppressing axis-dependent variance and exhibiting a monotonic degradation trend. Across five repeated measurement cycles, the MCCM preserved a consistent degradation trend and showed lower dispersion than the most variable individual RCR component, supporting its use as the primary scalar indicator for joint-condition tracking.
4. Synchronization rationale: The study demonstrates that temporal synchronization is a methodological prerequisite. Since both the MTRIF and pointwise RCR comparisons depend on continuous sample-level alignment, the CNSS principle is mandatory for maintaining a common master clock domain across independent nodes.
5. Integrated framework: The Thesis provides an experimentally grounded methodology integrating multidimensional excitation, paired 3DOF sensing, per-axis coherence evaluation, and metric fusion. This approach advances structural health monitoring toward localized, repeatable, and multiaxial assessment of structural joint integrity. The limitations of the current experimental validation and their implications for generalizability are discussed in Section 7.4.

7.2. Practical Recommendations

- Sensor alignment: Near and far sensors must be physically aligned along their corresponding $X, Y,$ and Z axes with secure mechanical coupling. This is necessary to

preserve the validity of the three linear-acceleration AMR pairs used for pointwise comparison [14].

- Excitation configuration: Actuator placement should be determined by the required diagnostic coverage. While the three-actuator configuration along $X, Y, \text{and } Z$ axes is sufficient for triaxial linear sensitivity, alternative configurations or additional actuators may be required if complex rotational coupling is expected.
- Synchronization continuity: Continuous sample-level alignment across excitation and sensing subsystems is mandatory. Without master-clock consistency, MTRIF focusing and RCR evaluation lose diagnostic reliability [31–33].
- Signal averaging: Repeated excitation and averaging are recommended to suppress uncorrelated noise and stabilize RCR and MCCM values [14, 15, 27]. High-rate multiaxial acquisition generates substantial data streams, necessitating robust data handling and labeling.
- Diagnostic indicators: MCCM should be utilized as the primary scalar indicator for joint condition tracking. Individual RCR values should be retained for directional diagnostic interpretation when detailed analysis of axis-specific degradation is required [12, 14, 15].

7.3. Further Development

Building on the findings and acknowledging the limitations discussed in Section 7.4, future studies should address the following technical areas.

- Automated axis alignment: Implementation of orientation-aware coordinate transformations to compensate for physical sensor misalignment mathematically.
- Adaptive MTRIF: Development of real-time transfer-function estimation to optimize the virtual impact focus under varying environmental conditions.
- Decentralized synchronization: Expansion of the CNSS protocol for large-scale sensor networks using wireless or PTP-based time distribution.
- Non-linear feature extraction: Integration of higher-order statistics into the MCCM fusion to improve sensitivity to micro-crack initiation.
- Edge computing implementation: Porting the RCR and MCCM algorithms directly to the FPGA for real-time, on-node joint integrity monitoring.

7.4. Limitations of the Current Study

The following limitations of the present study should be acknowledged to provide an accurate assessment of the framework's current state and to guide future development.

Single baseline joint configuration. The integrated framework is validated on a single structural steel joint (HEA 100 beams with one M16 bolt). While earlier experimental objects from the appended publications – including timber joints [15] and alternative steel configurations [12–14] – provide complementary evidence for individual methodological components, the full MTRIF–AMR–CNSS chain is demonstrated for a single joint geometry, material, and connection type. The extent to which the observed MCCM trends generalize to

different joint types (riveted, bonded, composite), materials, number of fasteners, or real-world boundary conditions remains to be established through a systematic validation campaign that covers multiple joint configurations.

Degradation emulation scope. The degradation sequence consists of controlled bolt-torque reduction that emulates stiffness loss due to loosened fasteners. While this is a widely used and repeatable approach in SHM research, it represents only one mode of degradation. Real-world structural joint degradation includes fatigue cracking, corrosion, delamination, and plastic deformation, each of which modifies the joint's dynamic behavior in different ways. The extent to which the MCCM responds to these alternative damage mechanisms, and whether the monotonic trend observed under torque reduction is preserved under other degradation modes, requires targeted experimental investigation.

Statistical characterization scope. The present validation includes five repeated measurement cycles for the same baseline joint configuration, which enables preliminary evaluation of RCR and MCCM repeatability through standard deviations. However, these repetitions were performed on a single specimen and under controlled laboratory conditions.

Therefore, the statistical characterization remains limited with respect to specimen-to-specimen variability, alternative joint geometries, different fastener layouts, and different degradation mechanisms. Future studies should extend the repeated-cycle analysis to multiple specimens and operating conditions and should include confidence intervals and formal monotonicity testing.

Sensitivity to non-ideal conditions. The current validation was performed under controlled laboratory conditions with careful sensor alignment, stable temperature, and no external loading. The sensitivity of the framework to practical deviations, such as sensor misalignment of several degrees, partial actuator failure, environmental temperature variation during measurement, or the presence of external operational loads, has not been systematically characterized. While the $\lambda/4$ criterion (Section 2.3) provides theoretical bounds, an experimental parametric study of robustness under non-ideal conditions would significantly strengthen confidence in the framework's applicability to field deployment.

These limitations do not diminish the methodological contributions of the Thesis, which lie in the formalization and initial experimental validation of the integrated MTRIF–AMR–CNSS framework. However, they define a clear agenda for the systematic validation and robustness characterization required before the methodology can be considered ready for practical deployment.

ACKNOWLEDGEMENT

I would like to express my sincere gratitude to all those who contributed to the successful completion of this research project.

First and foremost, I would like to thank my students Aleksandrs Mjakiševs, Aleksis Kurajevs, and Andrejs Macevičs, who actively participated in the experimental work and successfully defended their Master's theses. Their engagement, precision, and technical contributions were essential for the execution of key measurements presented in this Thesis.

Special thanks are extended to Dmitrijs Serdjuks, the principal investigator of the Latvian Council of Science project "Method of correlation of coaxial accelerations in 6-D space for quality assessment of structural joints" ("COACCEL**"** (Nr. lzp-2020/1-0240), for his sustained support and encouragement throughout the project.

I would also like to express my sincere gratitude to Professor Alexander Sutin and Professor Armen Sarvazyan for introducing me to the fascinating world of Time-Reversal Acoustics during my work at Artann Laboratories in the United States. Their ideas, inspiration, and scientific examples had a lasting influence on my research path and broadened my understanding of what is possible in this field.

I am particularly grateful to my supervisors, Jevgenijs Barkanovs, the principal investigator of the ERDF project "An Effectiveness Improvement of Conventional Pultrusion Processes" (project ID No. 1.1.1.1/18/A/053), in which I participated during my doctoral studies, and Aleksejs Tatarinovs, whose encouragement and guidance were instrumental in my decision to resume and complete doctoral studies. Their support opened the door to research opportunities that were both challenging and inspiring.

Most importantly, I wish to thank my family for their unwavering support throughout this journey. To my wife Karina, whose encouragement and understanding kept me moving forward when I was ready to stop. And to my sons, Nikita and Matvejs, who were born during this research and who, perhaps unknowingly, allowed me the time and space to pursue it.

Finally, I am thankful to all the individuals who participated in the experiments and contributed to the progress of this work.

REFERENCES

[1] Tol S, Özgüven HN. Dynamic characterization of bolted joints using FRF decoupling and optimization. Mech Syst Signal Process. 2015; 54–55:124–138. doi:10.1016/j.ymssp.2014.08.005.

[2] Zhan J, Zhang F, Siahkouhi M. A step-by-step damage identification method based on frequency response function and cross signature assurance criterion. Sensors. 2021; 21(4):1029. doi:10.3390/s21041029.

[3] Yang B, Xuan FZ, Xiang Y, Li D, Zhu W, Tang X, et al. Lamb wave-based structural health monitoring on composite bolted joints under tensile load. Materials. 2017; 10(6):652. doi:10.3390/ma10060652.

[4] Rucka M. Monitoring steel bolted joints during a monotonic tensile test using linear and nonlinear Lamb wave methods: a feasibility study. Metals. 2018; 8(9):683. doi:10.3390/met8090683.

[5] Xu J, Wang C, Li H, Zhang C, Hao J, Fan S. Health monitoring of bolted spherical joint connection based on active sensing technique using piezoceramic transducers. Sensors. 2018; 18(6):1727. doi:10.3390/s18061727.

[6] Zhang M, Tang Z, Yun CB, Sui X, Chen J, Duan Y. Bolt looseness detection using SH guided wave and wave energy transmission. Smart Mater Struct. 2021; 30(10):105015. doi:10.1088/1361-665X/ac1d90.

[7] Stolze FHG, Worden K, Manson G, Staszewski WJ. Fatigue-crack detection in a multi-riveted strap-joint aluminium aircraft panel using amplitude characteristics of diffuse Lamb wave field. Materials. 2023; 16(4):1619. doi:10.3390/ma16041619.

[8] Liang Y, Feng Q, Li D, Cai S. Loosening monitoring of a threaded pipe connection using the electromechanical impedance technique – experimental and numerical studies. Sensors. 2018; 18(11):3699. doi:10.3390/s18113699.

[9] Zhu J, Qing X, Liu Q, Liu X, Wang Y. Monitoring of fiber-reinforced composite single-lap joint with electromechanical impedance of piezoelectric transducer. Materials. 2019; 12(19):3241. doi:10.3390/ma12193241.

[10] Caldwell SP, Radford DW. Composite single lap shear joint integrity monitoring via embedded electromechanical impedance sensors. J Compos Sci. 2023; 7(2):53. doi:10.3390/jcs7020053.

[11] Caldwell SP, Radford DW. The health monitoring of bonded composite joints using both thickness and radial impedance resonance responses. Sensors. 2024; 24(8):2508. doi:10.3390/s24082508.

[12] Serdjuks D, Kurtenoks V, Tatarinovs A, Mironovs V, Lapkovskis V, Buka-Vaivade K, Macevics A, Topcijs K, Vilnitis M. Method of coaxial accelerations correlation for quality assessment of structural joints. Procedia Struct. Integr. 2022; 37:547–554. doi:10.1016/j.prostr.2022.01.121.

[13] Serdjuks D, Kurtenoks V, Tatarinovs A, Buka-Vaivade K, Lapkovskis V, Mironovs V, Podkoritovs A, Topcijs K. Non-model vibration analysis method for health monitoring of

structural joints. Procedia Struct. Integr. 2022; 37:555–562. doi:10.1016/j.prostr.2022.01.122.
[14] Buka-Vaivade K, Kurtenoks V, Serdjuks D. Non-destructive damage detection of structural joint by coaxial correlation method in 6D space. Buildings. 2023; 13(5):1151. doi:10.3390/buildings13051151.
[15] Kurtenoks V, Kurajevs A, Buka-Vaivade K, Serdjuks D, Lapkovskis V, Mironovs V, Podkoritovs A, Vilnitis M. The quality assessment of timber structural joints using the coaxial correlation method. Buildings. 2023; 13(8):1929. doi:10.3390/buildings13081929.
[16] Muttillo M, Stornelli V, Alaggio R, Paolucci R, Di Battista L, de Rubeis T, et al. Structural health monitoring: an IoT sensor system for structural damage indicator evaluation. Sensors. 2020; 20(17):4908. doi:10.3390/s20174908.
[17] Murray-Bergquist L, Bernauer F, Igel H. Characterization of six-degree-of-freedom sensors for building health monitoring. Sensors. 2021; 21(11):3732. doi:10.3390/s21113732.
[18] Fink M. Time reversal of ultrasonic fields. I. Basic principles. IEEE Trans Ultrason Ferroelectr Freq Control. 1992; 39(5):555–566. doi:10.1109/58.156174.
[19] Zeng L, Lin J, Huang L. A modified Lamb wave time-reversal method for health monitoring of composite structures. Sensors. 2017; 17(5):955. doi:10.3390/s17050955.
[20] Du F, Xu C, Wu G, Zhang J. Preload monitoring of bolted L-shaped lap joints using virtual time reversal method. Sensors. 2018; 18(6):1928. doi:10.3390/s18061928.
[21] Liang Y, Feng Q, Li D. Loosening monitoring of the threaded pipe connection using time reversal technique and piezoceramic transducers. Sensors. 2018; 18(7):2280. doi:10.3390/s18072280.
[22] Xu C, Wu G, Du F, Zhu W, Mahdavi SH. A modified time reversal method for guided wave-based bolt loosening monitoring in a lap joint. J Nondestruct Eval. 2019; 38:85. doi:10.1007/s10921-019-0626-1.
[23] Du F, Xu C, Zhang J. A bolt preload monitoring method based on the refocusing capability of virtual time reversal. Struct Control Health Monit. 2019; 26(8):e2370. doi:10.1002/stc.2370.
[24] Wang F, Song G. Bolt early looseness monitoring using modified vibro-acoustic modulation by time-reversal. Mech Syst Signal Process. 2019; 130:349–360. doi:10.1016/j.ymssp.2019.04.036.
[25] Panagiotopoulos CG, Stavroulakis GE. A numerical study on computational time reversal for structural health monitoring. Signals. 2021; 2(2):225–244. doi:10.3390/signals2020017.
[26] Sutin A, Kurtenoks V, Sabatier J, Burgett R, O'Neil M, Aranchuk S, et al. Time-reversal acoustic focusing of waves produced by seismic vibrators. J Acoust Soc Am. 2006; 120(5 Suppl):3369.
[27] Sutin A, Libbey B, Kurtenoks V, Fenneman D, Sarvazyan A. Nonlinear detection of land mines using wide bandwidth time-reversal techniques. Proc. SPIE 6217, 62171B (2006). doi:10.1117/12.673714.

[28] Fillinger L, Kurtenoks V, Rosenblum S, Sutin A, Sarvazyan A. Flexible tools for time reversal acoustics focusing applications. J Acoust Soc Am. 2007; 122(5 Suppl):3009. doi:10.1121/1.2942748.

[29] Fillinger L, Kurtenoks V, Lewis G Jr, Sutin A, Sarvazyan A. Time-reversal ultrasound system for enhanced drug delivery in the rat brain. In: Abstracts of the 9th International Symposium on Therapeutic Ultrasound; 2009 Sep; Aix-en-Provence, France. p. 105.

[30] Fu H, Sharif Khodaei Z, Aliabadi MHF. An event-triggered energy-efficient wireless structural health monitoring system for impact detection in composite airframes. IEEE Internet Things J. 2019; 6(1):1183–1192. doi:10.1109/JIOT.2018.2867722.

[31] Smetskaja V, Litvinenko A, Kurtenoks V, Stepanovs V, Lapkovskis V, Bespal'ko V. Study on thermal stability of multi-channel picosecond precise time-tagging system. In: 2023 IEEE 10th Jubilee Workshop on Advances in Information, Electronic and Electrical Engineering (AIEEE). 2023; 87–90. doi:10.1109/AIEEE58915.2023.10134855.

[32] Lapkovskis V, Litvinenko A, Kurtenoks V, Stepanovs V, Smetska V, Bespal'ko V. Multi-channel synchronization for picosecond time-tagging system. In: 2023 IEEE 10th Jubilee Workshop on Advances in Information, Electronic and Electrical Engineering (AIEEE). 2023; 81–86. doi:10.1109/AIEEE58915.2023.10134773.

[33] Bespal'ko V, Litvinenko A, Stepanovs V, Kurtenoks V, Smetska V, Lapkovskis V. Compensation of Accuracy Error for Time Interval Measurements. Latvian J Phys Tech Sci. 2024; 61(1):43–51. doi:10.2478/lpts-2024-0005.



Viktors Kurtenoks was born on 2 December 1969 in Tukums. He obtained a Bachelor's degree (1991) and a Master's degree (1992) in Computer Engineering from Riga Technical University (RTU). From 2001 to 2008, he worked as a senior software/hardware/firmware designer at Artann Laboratories (Trenton, USA). He is currently Chief Technical Officer at Eventech Ltd, one of the leading developers of event timers and time taggers, and Chief Technical Officer leading full-cycle development at his own companies Digits Ltd and Juvitek Ltd; he also works at RTU. He is a doctoral student in the Doctoral Study Programme "Civil Engineering" at RTU.

His expertise covers full product development from idea to functional unit, high-speed digital, analogue and mixed-signal electronics, ultra-fast ICs (ADC, DAC, memory), DSP, microcontrollers and FPGA/CPLD design in VHDL.